Sensing alterations of the local environment of 3d, 4d, and 4f central ions in polyoxopalladates with soft x-ray magnetic dichroisms

Carolin Schmitz-Antoniak[a,*], Natalya V. Izarova[a], Maria Stuckart[a,1], Alevtina Smekhova[a,2], Detlef Schmitz[b], S. Fatemeh Shams[a], Konrad Siemensmeyer[b], Margret Giesen[a], Paul Kögerler[a,c]

[a] *Peter-Grünberg-Institut (PGI-6), Forschungszentrum Jülich, 52425 Jülich, Germany*
[b] *Helmholtz-Zentrum Berlin für Materialien und Energie, Albert-Einstein-Str. 15, 12489 Berlin, Germany*
[c] *Institut für Anorganische Chemie, RWTH Aachen University, Landoltweg 1, 52074 Aachen, Germany*

Abstract

Polyoxopalladates hosting 3d, 4d or 4f central ions form a new class of molecular materials with well-defined, tunable morphology and ions coordination to be considered as model systems for basic research. We investigated the isotropic x-ray absorption near-edge structure (XANES), x-ray magnetic circular dichroism (XMCD), and x-ray magnetic linear dichroism (XMLD) to monitor the influence of symmetry changes on electronic and magnetic properties. After a brief introductory review about recent results on 3d and 4d transition metal ions, we (i) show that a change of the coordination symmetry from cubic eightfold (tetrahedral) to sixfold (octahedral) reduces the magnetic moment of Co^{2+} significantly and (ii) investigate whether axial distortions can modify the 4f states of trivalent lanthanide ions. While for Gd^{3+} there is no effect visible within experimental uncertainties, changes were observed for Dy^{3+} and Ho^{3+}. The results are compared to atomic multiplet calculations including the intra-atomic spin-dipole term $\langle T_z \rangle$. Furthermore, several experimental pitfalls are discussed that may lead to misinterpretation of x-ray absorption data but can be excluded in the present study.

Keywords: x-ray absorption; XMCD; molecular magnets; polyoxometallates; d metal ions; lanthanides

*Corresponding author
Email address: c.schmitz-antoniak@fz-juelich.de (Carolin Schmitz-Antoniak)
[1] present address: Institut für Chemische Reaktionstechnik, Friedrich-Alexander-Universität Erlangen-Nürnberg, Egerlandstr. 3, 91058, Erlangen, Germany
[2] present address: Helmholtz-Zentrum Berlin für Materialien und Energie, Albert-Einstein-Str. 15, 12489 Berlin, Germany

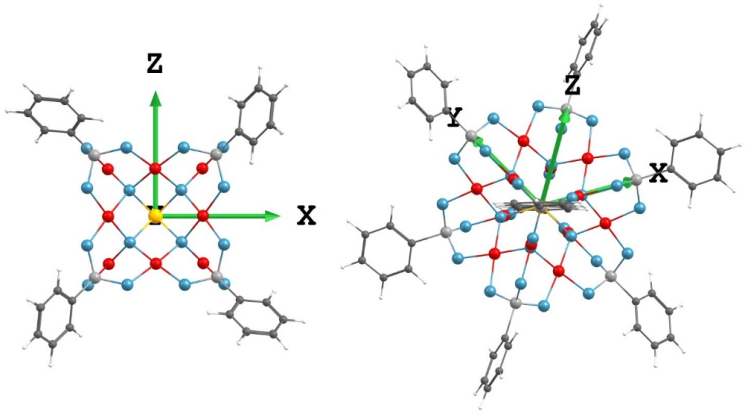

Figure 1: Ball-and-stick representation of MPdPhAs from two different perspectives. Color code: yellow - central (3d, 4f) ion, blue - oxygen, red - palladium, grey - arsenicum, dark grey - carbon, white - hydrogen. An animated 360° rotation accompanies the online version of this paper.

1. Introduction

Polyoxopalladates (POP) form a new class of molecular materials, which gained a lot of interest due to their various possible applications e.g. as noble metal-based catalysts [1, 2, 3], hydrogen uptake and sensing materials [4] or spin qubits [5]. Their general formula can be written as $[MPd^{II}_{12}O_8L_8]^{n-}$ consisting of a central metal ion (M) in a cuboid dodecapalladate shell and stabilized by eight capping groups (L) as sketched in Fig. 1 for L = $PhAsO_3$ (phenyl arsonate, PhAs). The first example of POP was discovered in 2008 [1]. It is composed of a central palladium(II) ion surrounded by a distorted cubic shell of twelve palladium(II) ions in square-planar oxygen coordination environments and capped by eight arsenate heterogroups. A few years later, a novel family of POP was discovered with 3d and 4f transition metal ions in the center and various capping groups, e.g. phosphate [6] and phenylarsonate [7, 8]. An overview of different structural types of polyoxopalladates and a discussion about mutual influences between central ions and hosting shells can be found in the work of Yang and Kortz [9]. In Table 1, the initial samples discussed in this work and their mean M–O bond lengths are listed.

1.1. Central 3d–O bond lengths

The bond lengths M–O between the central metal ion and the surrounding oxygen anions is not only influenced by the size of the ion, but can be tuned by the prosthetic capping groups at the outside of the MPd_{12} cluster. As a rule of thumb, capping groups L = RXO_3 with longer X–O bond lengths cause an expansion of the dodecapalladate nanocube hosting the central ion and,

Label	Composition	Central ion	Bond length (Å)	Ref.
FePdP	$[Fe^{III}O_8Pd^{II}_{12}(P^{V}O_4)_8]^{13-}$	Fe^{3+}	2.206	[6]
FePdPhAs	$[Fe^{III}O_8Pd^{II}_{12}(PhAs^{V}O_3)_8]^{5-}$	Fe^{3+}	2.224	[8]
CoPdP	$[Co^{II}O_8Pd^{II}_{12}(P^{V}O_4)_8]^{14-}$	Co^{2+}	2.234	[6]
CoPdP-H/O		Co^{2+}	n.a.	[4]
CoPdPhAs	$[Co^{II}O_8Pd^{II}_{12}(PhAs^{V}O_3)_8]^{4-}$	Co^{2+}	2.259	[8]
CoPdPhAs-2CD		Co^{2+}	2.276	[10]
GdPdPhAs	$[Gd^{III}O_8Pd^{II}_{12}(PhAs^{V}O_3)_8]^{5-}$	Gd^{3+}	2.379	[7]
GdPdPhAs-2CD		Gd^{3+}	n.a.	
DyPdPhAs	$[Dy^{III}O_8Pd^{II}_{12}(PhAs^{V}O_3)_8]^{5-}$	Dy^{3+}	2.335	[7]
DyPdPhAs-2CD		Dy^{3+}	n.a.	
HoPdPhAs	$[Ho^{III}O_8Pd^{II}_{12}(PhAs^{V}O_3)_8]^{5-}$	Ho^{3+}	2.349	[7]
HoPdPhAs-2CD		Ho^{3+}	n.a.	
PdAs	$[Pd^{II}_{13}As^{V}_8O_{34}(OH)_6]^{8-}$	Pd^{2+}	2.020	[1]

Table 1: Sample labelling, chemical composition of parental POP cluster, and central ions studied and discussed in this work as well as mean bond lengths between central metal ion and surrounding oxygen anions.

consequently, larger M–O distances. Let us choose Fe^{3+} as an example for the central ion. For phenylarsonate capping groups, the mean Fe–O distance is 2.224 Å [8], which is about 1% larger than for the case of phosphate capping groups (2.206 Å [6]). Compared to Fe containing POP stabilized by selenite capping groups (Fe–O distance of 2.149 Å [8]), the increase is even about 3.5%. The enhanced bond length leads to a lower energy of the lowest unoccupied molecular orbital, which has an important influence on the reduction behaviour in catalytic processes or hydrogen detection. For instance, a soft hydrogen plasma treatment of FePdPhAs leads to a reduction of Fe^{3+} central ions to metallic Fe, while for FePdP the reduction process yields Fe^{2+} [4].

Regarding the magnetic properties of the central ion in the as-prepared states, only subtle changes due to different bond lengths are present. Since the eightfold coordination symmetry is connected to moderate crystal field splittings of the orbitals, all samples are in the high-spin configuration.

1.2. Pd–O bonds in the shell

For the Pd^{2+} ions in the shell, at a first glance the magnetic properties do not change in this regime of bond lengths. In all samples, the ions with a $4d^8$ electron configuration show a diamagnetic response to an external magnetic field due to the large crystal field splitting caused by the square-planar coordination symmetry: Since only the lobes of the $d_{x^2-y^2}$ orbital point directly to the negatively charged oxygen anions, it is energetically unfavoured and remains unoccupied. Thus, the ground state is diamagnetic ($\langle S_z \rangle = 0$).

In addition, with x-ray absorption spectroscopy it was recently found that the electronic structure is affected by the bond length: While for short Pd–O bond lengths (in FePdP or CoPdP) the ground state can indeed be described

by an unoccupied $d_{x^2-y^2}$ orbital as expected in this simple picture, for larger bond lengths connected to PhAs capping groups the large spin-orbit coupling of Pd facilitates another ground state in which two electrons with opposite spin are related to formally different orbitals, i.e. $d_{x^2-y^2}$ and d_z^2 [11].

1.3. Modifications of the coordination symmetry

By attaching two α-cyclodextrin ($[C_{36}H_{60}O_{30}]^{6-}$, CD) molecules, it has been shown that it is even possible to change the coordination symmetry of the central ion [10]. In more detail, the non-covalent interactions between the POP and two trans-positioned CD moieties alter the eightfold coordination environment of central Co^{2+} ions by inducing an axial distortion of the otherwise cubic polyoxopalladate environment. This effectively leads to an elongation of the bonds along the cube diagonal, i.e. in the plane located between the two CD molecules. With x-ray absorption spectroscopy the related change of the symmetry towards trigonal could be clearly seen from the reduction of the XMLD signal [10].

In the case of Pd^{2+} in the centre of PdAs POP, it was shown that additional oxygen anions close to the coordination environment can modify the magnetic response: Although the central ion is formally coordinated in a square-planar symmetry like the ones in the dodecapalladate shell and consequently were expected to be diamagnetic, four additional oxygen anion in close vicinity lead to paramagnetism [11].

These results already justify proposing POP as molecular model systems for x-ray absorption spectroscopy due to their well-defined structure and tuneable properties. In the present study, we (i) studied the magnetic properties of Co^{2+} ions in further different coordination symmetries (eightfold (T_d) or sixfold (O_h) coordinated) and (ii) investigated if 4f states of lanthanide ions are measurably affected by a distortion induced by two CD molecules attached as described above for the 3d states of Co^{2+}. For this purpose, we analyzed the isotropic x-ray absorption near-edge structure (XANES), its associated magnetic circular dichroism (XMCD) and magnetic linear dichroism (XMLD) of Gd^{3+}, Dy^{3+}, and Ho^{3+} in cubic or distorted cubic environments. The results are interpreted by comparison with atomic multiplet calculations.

2. Sample preparation and topography

Details about the synthesis of different POP samples can be found either in the cited references in Table 1 or in the Supplementary Material. For x-ray absorption spectroscopy investigations, the dried powder samples were re-dispersed in purified water with a concentration in the range of 10^{-9} mol/l and drop coated on freshly cleaved highly oriented pyrolytic graphite (HOPG) substrates. The samples were carefully heated to about 50°C to accelerate the evaporation of water without the risk of thermal decomposition of the POP. As discussed in the Supplementary Material, the preparation on HOPG prevents the spectra from artificial line broadening by charging effects (Fig. S5).

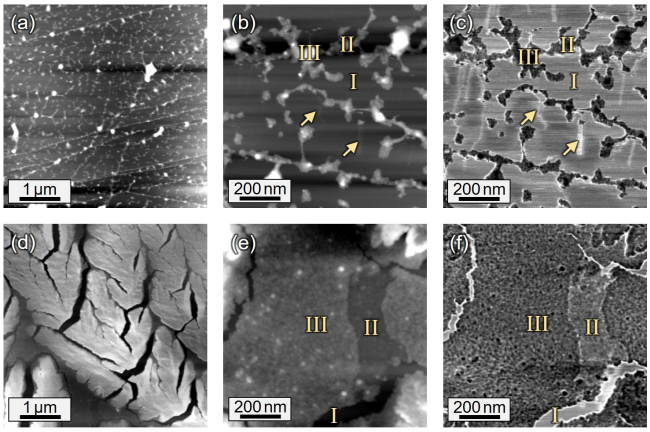

Figure 2: Atomic force microscopy of FePdP on HOPG (top row) and FePdPhAs (bottom row) on HOPG. Images (a), (d) show the topographies of 5×5 μm^2 large areas with typical coverage; (b), (e) show the topography zoomed in on a 1×1 μm^2 large area and (c), (f) the corresponding phase images.

Atomic force microscopy (AFM) images reveal that the coverage of the HOPG substrate depends on the capping group of the POP and related adhesion. In Fig. 2(a) a topography image of a 5×5 μm^2 large area of FePdP on HOPG is shown. One can clearly see that during the drying process, FePdP formed agglomerates connected by thin lines of FePdP in a monolayer coverage. Line scans indicate the height of the crystals to be typically in the range of $2 - 4$ nm corresponding to a few monolayers. Fig. 2(b) and (c) show the amplitude (topography) and phase contrast image, respectively, of a 1×1 μm^2 large area. Due to different surface softness and adhesion between the AFM tip and the surface, in the phase contrast image the empty HOPG substrate appears light grey (I), while the areas covered with FePdP are darker and correspond to a monolayer of FePdP (II) or larger agglomerates (III). Due to the low adhesion between FePdP and HOPG, some small FePdP crystals were moved by the scanning AFM tip leading to some artifacts in the images that appear as bright structures, two examples are marked by arrows. Increasing the concentration leads to a larger fraction of the monolayered connections between agglomerates (not shown here).

In Fig. 2(d)-(f), corresponding topography and phase images are shown for FePdPhAs. Already on the larger scale significant differences are apparent as some dendritic structures can be observed, which are not obtained for the FePdP sample. The overall coverage seems to be more homogeneous, i.e. large areas are covered by a monolayer or two monolayers as can be seen in particular by the phase contrast in Fig. 2(f). Again, the light grey (I) corresponds to empty HOPG, but only small uncovered areas are visible. Darker grey corresponds to a monolayer (II) and double-layers (III) of FePdPhAs. A few dark spots are

related to larger crystals.

3. Further methods

3.1. X-ray absorption spectroscopy

Experiments were carried out in the high-field end station at beamline UE46-PGM1 of the HZB-BESSY II synchrotron radiation source. The undulator beamline offers monochromatic x-rays in the soft x-ray range with variable polarization. In order to resolve spectral fine structures, the instrumental line broadening should be smaller than the life-time broadening of the system studied. Here we used an exit slit width of 20 μm leading to an instrumental broadening of about 100 meV at the energy of the Fe L_3 absorption edge. Measurements were carried out in normal x-ray incidence. For XMCD measurements, the magnetic field was applied parallel to the k vector of incoming left or right circularly polarized x-rays. For XMLD measurements with linearly polarized x-rays the magnet was rotated by 90°. To increase the total electron yield in this geometry, the sample was tilted by 8° away from normal x-ray incidence. For vertical polarization, the axis of the electric field vector of the x-rays is again perpendicular to the magnetic field vector, while for horizontal polarization the two vectors are collinear. The intensities of the x-ray absorption are denoted I^+ (I^-) for positive (negative) helicity and $I^{\parallel}$ ($I^{\perp}$) for horizontal (vertical) linear polarization. Isotropic XANES, XMCD, and XMLD are calculated after proper normalization of the spectra according to:

$$I_{XANES} = (I_n^+ + I_n^- + I_n^{\parallel})/3 \tag{1}$$

$$I_{XMCD} = (I_n^+ - I_n^-)/P \tag{2}$$

$$I_{XMLD} = I_n^{\perp} - I_n^{\parallel} \tag{3}$$

where the index n denotes normalized spectra and P is the degree of circular polarization (here, 0.9). Measurements were performed in the energy range 760 eV$\leq E \leq$840 eV for Co $L_{3,2}$ absorption edges, 1165 eV$\leq E \leq$1250 eV for Gd $M_{5,4}$ absorption edges, 1270 eV$\leq E \leq$1365 eV for Dy $M_{5,4}$ absorption edges, and 1315 eV$\leq E \leq$1420 eV for Ho $M_{5,4}$ absorption edges. For the case of Dy and Ho a background spectrum of the As $L_{3,2}$ absorption edges was measured on GdPdPhAs in the corresponding energy ranges and subtracted. More details about the data treatment can be found in the Supplementary Material.

3.2. Atomic multiplet calculations

In order to qualitatively verify the experimental observations, full atomic multiplet calculations were performed using the Quanty program [12, 13]. Input files were generated with the help of Crispy software [14]. The local ansatz of multiplet theory is suited to calculate the initial states of both 3d transition metal and lanthanide ions as well as core-level x-ray absorption spectra studied here. By default Slater integrals were reduced to 80% of the

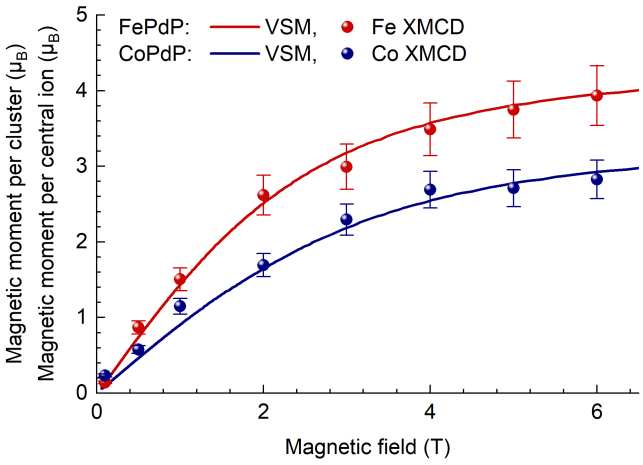

Figure 3: Magnetic moments per polyoxopalladate cluster determined from VSM magnetometry of FePdP (red line) and CoPdP (blue line) powder and element-specific total magnetic moment per central ion determined from XMCD of Fe (red symbols) and Co (blue symbols) in FePdP and CoPdP, respectively, as a function of external magnetic field.

respective Hartree-Fock value, otherwise it is mentioned in the text. A magnetic field as quantization axis was included along the z direction with $B_x = B_y = 0$ and $B_z = 6\,\mathrm{T} \approx 0.35\,\mathrm{meV}$ as used in the experiment. To generate XMCD spectra, the k vector of incoming x-rays was parallel to the magnetic field along the z axis, while for XMLD spectra the magnetic field was set along the y direction ($B_x = B_z = 0$, $B_y = 6\,\mathrm{T}$). In this geometry the natural linear dichroism is minimized for the lanthanide ions, which cancels out in the experiment due to random orientations of the crystal axes.

In particular for the case of the lanthanide 4f states the crystal field splitting and Zeeman energy level splitting in a magnetic field is in the range of thermal energy. The population of different eigenstates i was considered following a Boltzmann distribution with relative occupation numbers

$$\mathrm{d}Z_i \propto \exp\left[-(E_i - E_1)/k_B T\right]. \tag{4}$$

3.3. Magnetometry

Magnetometry measurements of polycrystalline powder samples were carried out in the CoreLab Quantum Materials at the Helmholtz-Zentrum Berlin using a vibrating sample magnetometer (VSM, Quantum Design) with maximum magnetic field of 14 T. To determine the magnetic moments per palladate cluster, the sample weights were determined by a microbalance and the numbers of clusters were calculated using their molar masses.

The magnetic response measured by magnetometry is clearly dominated by the paramagnetic central ions as can be seen by comparison of VSM data of FePdP and CoPdP with magnetic field dependent element-specific magnetic

Ion	Coord.	$\langle J_z \rangle$	$\langle L_z \rangle$	$\langle S_z \rangle$	$\langle T_z \rangle$	dZ (%)
Co^{2+}	8-fold (T_d)	-1.909	-0.417	-1.492	≈ 0	86.8
Co^{2+}	6-fold (O_h)	-1.465	-0.604	-0.861	0.005	98.2

Table 2: Ion label, coordination, calculated expectation values $\langle J_z \rangle$, $\langle S_z \rangle$, $\langle L_z \rangle$ as well as magnetic dipole term $\langle T_z \rangle$ for experimental conditions, i.e. $T = 4.5\,\mathrm{K}$, $B_z = 6\,\mathrm{T}$, and corresponding relative thermal occupation dZ. Crystal field parameters as mentioned in the text and reduction of Slater integrals (to 72% of the Hartree-Fock value) have been taken from Ref. [4].

moments of Fe or Co as determined from XMCD (3): The VSM data are the same as presented in Ref. [11] and are in good agreement with the magnetic moments determined from XMCD. Furthermore, no difference between magnetic field dependent and (reciprocal) temperature dependent magnetic moment measured with VSM was obtained as expected for dominant Langevin paramagnetism.

4. Magnetism of Co^{2+}: From eightfold to sixfold coordination

In the as-prepared state of CoPdP, the central Co^{2+} ion is eightfold coordinated by oxygen anions. By hydrogenation and subsequent re-oxidation this coordination symmetry changed to a common octahedral oxygen environment with six nearest neighbours [4] as sketched in the insets of Fig. 4. This gives the possibility to investigate the same Co^{2+} ions in different coordinations by the same ligand (oxygen). The change of symmetry is connected to a re-arrangement of the orbital occupation: The cubic eightfold coordination can be formally described by a tetrahedral symmetry with two oxygen anions on each surrounding site. In the single-electron picture, this is connected to a lower energy of the two e_g states ($\mathrm{d}_{x^2-y^2}$, d_{z^2}) with respect to the three t_{2g} states (d_{xz}, d_{yz}, d_{xy}), while in octahedral symmetry the t_{2g} states are energetically favoured. In both cases, the energy splitting of the d orbitals is so small that the central ion is in the high-spin state. For Co^{2+} it was found from specific changes in the isotropic XANES to be $10Dq = (-0.62 \pm 0.05)\,\mathrm{eV}$ (tetrahedral) and $10Dq = (1.1 \pm 0.2)\,\mathrm{eV}$ (octahedral) [4]. Here, we studied in addition the XMCD to reveal possible changes in the magnetic moments due to the orbital re-occupation and present the effects of XMLD on the absorption fine structures.

From the calculated initial-state expectation values presented in Table 2, the total magnetic moment which is dominated by the spin magnetic moments $m_S \approx -2\,\langle S_z \rangle\,\mu_B$ is expected to be smaller in octahedral symmetry. The orbital contribution $\langle L_z \rangle$ is enhanced and the spin dipole term $\langle T_z \rangle$ is larger in octahedral symmetry as well, but still quite small. Note that for other ions, e.g. lanthanide ions, the $\langle T_z \rangle$ term may be orders of magnitude larger and cannot be neglected even for randomly oriented crystallographic axes as will be discussed later.

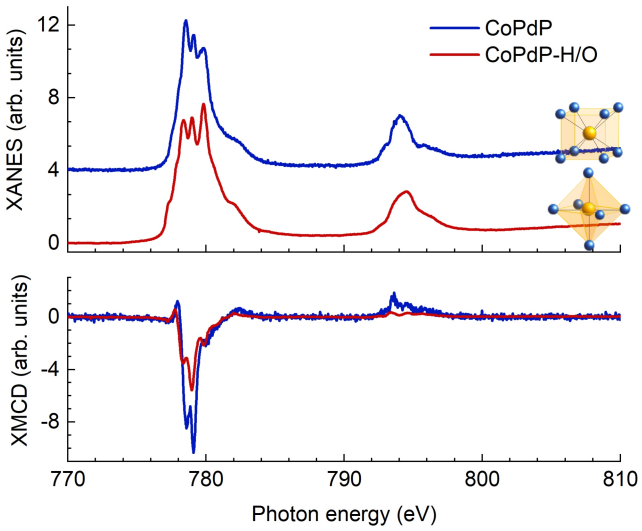

Figure 4: Isotropic x-ray absorption near-edge structure (XANES, top panel) and magnetic circular dichroism (XMCD, bottom panel) of Co^{2+} ions eightfold coordinated (blue) or sixfold coordinated (red) by oxygen anions measured at $T = 4.5$ K and $B = 6$ T. For clarity, a vertical offset has been added. The corresponding coordination symmetries are sketched in the top panel.

The experimental isotropic XANES and XMCD spectra are presented in Fig. 4 for CoPdP in the as-prepared (T_d) state and after hydrogenation and subsequent re-oxidation labelled CoPdP-H/O. After this treatment the spectra are less noisy because of a better electric conductivity of the sample. For both samples the isotropic XANES exhibits the typical fine structure of Co^{2+}, but with different peak intensities related to changes in coordination number and symmetry as already discussed in Ref. [4]. Note that the isotropic XANES cannot be obtained by simply averaging the absorption spectra measured with reversed x-ray circular polarizations in the large magnetic field as used for XMCD. Since the electric field vector of incident x-rays is always perpendicular to the magnetic field in the XMCD measurement geometry, the average $\bar{I}_n^{circ} = (I_n^+ + I_n^-)/2$ includes magnetic linear dichroism. If a rotation of the magnetic field to obtain the XMLD in a well-defined manner is not possible, a simple method to obtain the isotropic XANES for paramagnetic samples like POP is to repeat the measurements without magnetic field applied or with a magnetic field close to zero. (The latter may be advantageous in some measurement geometries to increase the TEY by the Lorentz force.)

Fig. 5 shows a comparison of the averaged spectra $\bar{I}_n^{circ}$ measured in a magnetic field of 6 T and the isotropic XANES at the Co L_3 edges for the two samples, i.e. CoPdP in the as-prepared state (a) and CoPdP-H/O (b). The differences between the averaged spectra in XMCD geometry in a magnetic field

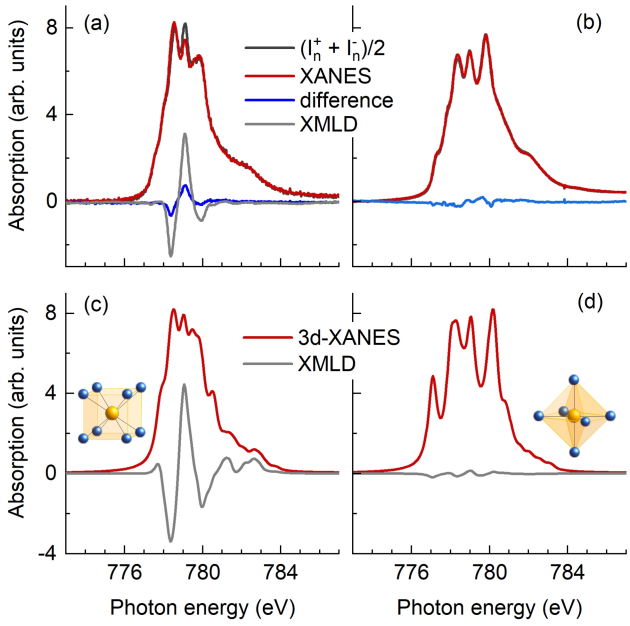

Figure 5: Comparison between averaged spectra using circular polarized x-rays in a magnetic field in XMCD measurement geometry (dark grey lines) and isotropic XANES (red lines) for eightfold coordinated Co^{2+} in CoPdP in the as-prepared (T_d) state (a) and sixfold coordinated Co^{2+} with O_h coordination symmetry (b) after hydrogenation and subsequent re-oxidation. Blue lines show the difference between the averaged spectra and isotropic XANES which is related to the magnetic linear dichroism which has been measured as well for CoPdP (grey line, data from Ref. [4]). Simulated 3d-XANES and XMLD spectra for the two different coordination symmetries, i.e. T_d and O_h are shown in (c) and (d), respectively.

of 6 T and the isotropic XANES spectra are shown as blue lines and are related to the XMLD as can be seen for the case of CoPdP (a). While for the Co^{2+} ions in the as-prepared state with eightfold coordination in T_d symmetry the averaged spectrum $\bar{I}_n^{circ}(6\,\mathrm{T})$ clearly shows a different ratio of peak intensities of the fine structure compared to the isotropic spectrum, there are only small changes for Co^{2+} ions in sixfold coordination with O_h symmetry.

The fine structure and the magnetic linear dichroism originate from multiplet effects, ligand fields, exchange and spin-orbit interactions [15] and are very sensitive to the local surrounding. For the case of Co^{2+} central ions in POP it has already be shown that the XMLD is strongly reduced for the case of axial distortion of the initial T_d symmetry, while the overall shape of the XMLD as well as the shape of the isotropic XANES is basically maintained [10]. Here, changing the symmetry towards O_h leads to a different spectral shape of both XMLD and isotropic XANES. This experimental finding is again qualitatively supported by atomic multiplet calculations (Fig. 5, c, d).

In addition, the line broadening for the experimental data of Co^{2+} ions in octahedral symmetry is larger than in the as-prepared (T_d) state. Since

the instrumental line broadening was the same for both measurements, this behaviour suggests a larger life-time broadening of the e_g-like states compared to the t_{2g}-like states.

The spectral shape of the XMCD looks very similar for the two samples, but the intensity is significantly lower for the CoPdP-H/O sample with respect to the as-prepared state pointing towards a smaller total magnetic moment in agreement with calculations. The effective spin and orbital magnetic moments, m_s^{eff} and m_l, can be quantified using the so-called sum rules [16, 17, 18]:

$$m_s^{\text{eff}} = -\frac{3p - 2q}{r}\ n_h\ \mu_B \tag{5}$$

$$m_l = -\frac{2q}{3r}\ n_h\ \mu_B \tag{6}$$

where p (q) denotes the integral of the XMCD spectrum over the L_3 (L_3 + L_2) absorption edge, r the integrated 3d-XANES intensity, which is obtained from the isotropic XANES by subtraction of a two step-like function accounting for electron transitions into higher unoccupied final states or the continuum, and n_h is the number of unoccupied final states, which is proportional to r. More details about the data treatment and all integrals can be found in the Supplementary Material. In sixfold coordinated O_h symmetry, the value of r was found to be larger with respect to the one of the eightfold coordinated as-prepared state. Assuming $n_h = 3$ for the as-prepared state, the proportionality $r \propto n_h$ yields a number of unoccupied final states of 3.7 in the modified symmetry, which was used to calculate the magnetic moments. In this case, we have not only a good agreement between theory and experiment, but also a good agreement with previously published magnetic moments, for which the integrated 3d-XANES of Fe^{3+} ($n_h = 5$) was used as a reference [4]. The resulting effective spin and orbital magnetic moments are presented in Table 3 and compared to the spin and orbital magnetic moments corresponding to the calculated expectation values (Tab. 2) according to

$$m_s^{\text{eff}} = -2\,\langle S_z \rangle - 7\,\langle T_z \rangle\ \mu_B \tag{7}$$

$$m_l = -\,\langle L_z \rangle\ \mu_B \tag{8}$$

For both symmetries, there is a reasonable agreement between magnetic moments determined from experimental data and results from atomic multiplet calculations. Note that in particular for the case of Co^{2+} in the as-prepared state, the orbital magnetic moment derived from experimental data is quite sensitive to the integration range: If the integration range is too small, it will be overestimated (and the effective spin magnetic moment slightly underestimated). Similar to what has been suggested for oxides like Fe_3O_4 [19], the integral value q which enters the sum-rules has been taken at an energy about 40 eV above the Co L_2 absorption edge. The integral values as a function of energy are shown in Figs. S7-S10 of the Supplementary Material.

	m_s^{eff} (μ_B)	m_l (μ_B)	m_{tot} (μ_B)	m_l/m_s^{eff}
exp. CoPdP	2.88 ± 0.5	0.78 ± 0.08	3.66 ± 0.5	0.27
theo. $Co^{2+}(T_d)$	2.984	0.417	3.401	0.14
exp. CoPdP-H/O	1.57 ± 0.3	0.61 ± 0.06	2.18 ± 0.3	0.39
theo. $Co^{2+}(O_h)$	1.687	0.604	2.326	0.36

Table 3: Effective spin, orbital and total magnetic moment as well as ratio of orbital to effective spin magnetic moment from experimental data and calculations.

5. The 4f states of lanthanide ions Ln^{3+}

The initial electron configuration of trivalent lanthanide (Ln^{3+}) ions is $[Xe]4f^n$, which is energetically well separated from the excited $[Xe]4f^{n-1}5d^1$ state. Furthermore, the localized 4f states are shielded by the expanded $5s^25p^6$ states that act like a Faraday cage. Hence, the sensitivity of 4f states to the local environment is weak and the crystal field is commonly treated as a pertubation. By appropriate parametrization, it can be formally written as a projection on the ground atomic multiplet according to [20, 21]

$$H_{CF} = \sum_{k,q} \alpha_n B_k^q O_k^q(J) \tag{9}$$

with the projection coefficient α_n and crystal field parameters B_k^q of rank $k = 2, 4, 6$ for the 4f states. The O_k^q describe the 4f wave functions in an analytical form as combinations of spherical harmonics. In the case of parental POP, which are highly symmetric in the as-prepared state, a description of the crystal field by the axial terms B_4^0 and B_6^0 is sufficient. Although the influence of the crystal field on the 4f states is expected to be small, we studied isotropic XANES, XMCD, and XMLD at the $M_{5,4}$ absorption edges, i.e. probing the 4f final states, of GdPdPhAs, DyPdPhAs, and HoPdPhAs with and without CD molecules attached. In this section, we firstly present the initial state properties from calculations and magnetometry measurements of the parental species, before presenting and discussing the (non-)influence of distorted symmetry by two attached CDs as obtained from x-ray absorption spectroscopy methods.

5.1. Initial state properties

Calculated expectation values $\langle S_z \rangle$, $\langle L_z \rangle$, and $\langle J_z \rangle$ in a magnetic field along the z direction of 6 T for the thermally populated eigenstates at $T = 5\,\text{K}$ with relative occupations $\text{d}Z > 1\,\%$ are listed in Table 4. The complete list of states including eigenstate energies can be found in Tables S1-S3 of the Supplementary Material. The values of the lowest eigenstates are close to the ones expected from Hund's rules for a free ion. In addition, the expectation value of the magnetic dipole term $\langle T_z \rangle$ is presented, which enters the effective spin magnetic moment obtained from XMCD analysis. The values of the energetically lowest eigenstates are in excellent agreement to values published by Teramura et al.

	state	$\langle J_z \rangle$	$\langle L_z \rangle$	$\langle S_z \rangle$	$\langle T_z \rangle$	dZ (%)
Gd^{3+}	1	-3.500	-0.035	-3.465	0.010	79.9
Gd^{3+}	2	-2.500	-0.028	-2.475	0.007	16.1
Gd^{3+}	3	-1.500	-0.015	-2.485	0.004	3.2
Dy^{3+}	1	-7.500	-5.083	-2.417	0.128	65.6
Dy^{3+}	2	-6.500	-4.405	-2.095	0.111	22.5
Dy^{3+}	3	-5.500	-3.723	-1.773	0.094	7.8
Dy^{3+}	4	-4.500	-3.049	-1.451	0.077	2.7
Ho^{3+}	1	-8.000	-6.084	-1.916	-0.137	63.2
Ho^{3+}	2	-7.000	-5.323	-1.677	-0.120	23.3
Ho^{3+}	3	-6.000	-4.563	-1.437	-0.103	8.6
Ho^{3+}	4	-5.000	-3.802	-1.198	-0.086	3.2
Ho^{3+}	5	-4.000	-3.041	-0.959	-0.069	1.2

Table 4: Calculated expectation values $\langle J_z \rangle$, $\langle S_z \rangle$, $\langle L_z \rangle$ as well as magnetic dipole term $\langle T_z \rangle$ for experimental conditions, i.e. $T = 5\,\mathrm{K}$, $B_z = 6\,\mathrm{T}$, and relative thermal occupations dZ of the relevant energy levels for Gd^{3+}, Dy^{3+}, and Ho^{3+}. Slater integrals were reduced to 80% of the Hartree-Fock values, no crystal field was considered. Full lists of states can be found in the Supplementary Material.

[22] and reflect the asphericity of the spin density distribution of the different 4f orbitals. For Gd^{3+} with its half-filled 4f shell, $\langle T_z \rangle$ is approximately zero, but becomes sizeable for Dy^{3+} and Ho^{3+}. The change of the sign between Dy^{3+} and Ho^{3+} marks a transition from a more oblate to prolate shape of the spin density distribution. In the XMCD spin sum rule for the 4f states ($M_{5,4}$ absorption edges), the $\langle T_z \rangle$ term enters the effective spin magnetic moment according to

$$m_s^{\mathrm{eff}} = -2\,\langle S_z \rangle - 3\,\langle T_z \rangle\ \mu_B \tag{10}$$

Note the different pre-factor of 3 compared to 7 for the case of 3d states ($L_{3,2}$ absorption edges).

The contribution of $\langle T_z \rangle$ of POP samples is much smaller, because the crystallographic axes are randomly distributed. But due to the large spin-orbit coupling of the 4f states, $\langle T_z \rangle$ does not cancel out [23]. In a simple picture, the spin-density distribution partially aligns via spin-orbit coupling with respect to the magnetic field. This contribution is always present, does not cancel out for randomly oriented crystals and cannot be determined from angular dependent XMCD of single-crystalline material.

Field-dependent magnetometry data at $T = 4\,\mathrm{K}$ of the parental GdPdPhAs, DyPdPhAs, and HoPdPhAs POP are presented in Fig. 6. For GdPdPhAs the magnetic moment per cluster approaches the saturation value of 7 μ_B very closely in the high-field region, whereas for DyPdPhAs and HoPdPhAs there is still a visible increase of the magnetic moment. This is expected for a Langevin paramagnet with larger J_z like Dy^{3+} and Ho^{3+}. Note that a high-field slope of the magnetic moments can also occur in powder samples if the POP align with the external magnetic field by rotation of the crystallites, which is a typical

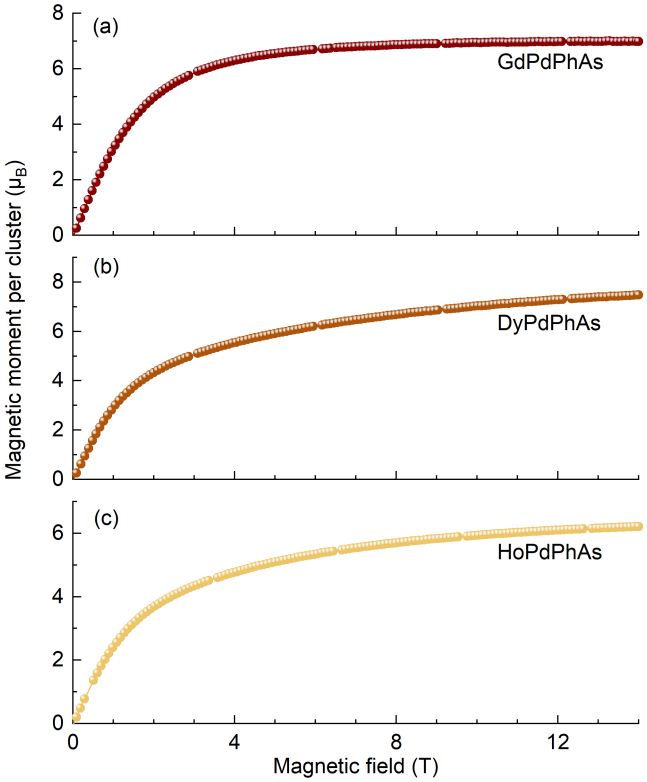

Figure 6: Magnetic field dependent magnetometry data at $T = 4\,\mathrm{K}$ of GdPdPhAs (a), DyPdPhAs (b), and HoPdPhAs (c). Every 20th data point is plotted.

problem for measuring lanthanides with large orbital magnetism and connected anisotropy. It can be overcome by pressing the powder as done in this work or by mixing it with glue or a liquid with a very high viscosity capable to prevent rotation of the crystallites.

5.2. Influence of symmetry modifications on 4f states

To answer the question raised in the beginning, whether the 4f states are affected by the changes of the local symmetry around the trivalent lanthanide ion, isotropic XANES, XMCD, and XMLD have been measured for the parental POP as well as after attaching two trans-positioned CD molecules. The spectra are shown in Fig. 7. Obviously, the strong change particularly in the XMLD reported for the $L_{3,2}$ absorption edges of Co^{2+} central ions [10] does not occur for the lanthanides. Calculated spectra are shown for comparison. Note that XANES, XMCD, and XMLD were scaled arbitrarily to match the peak heights at the M_5 absorption edge of the experimental spectra. The spectral shapes of all lanthanide POPs investigated here experimentally, match very well calculated spectra.

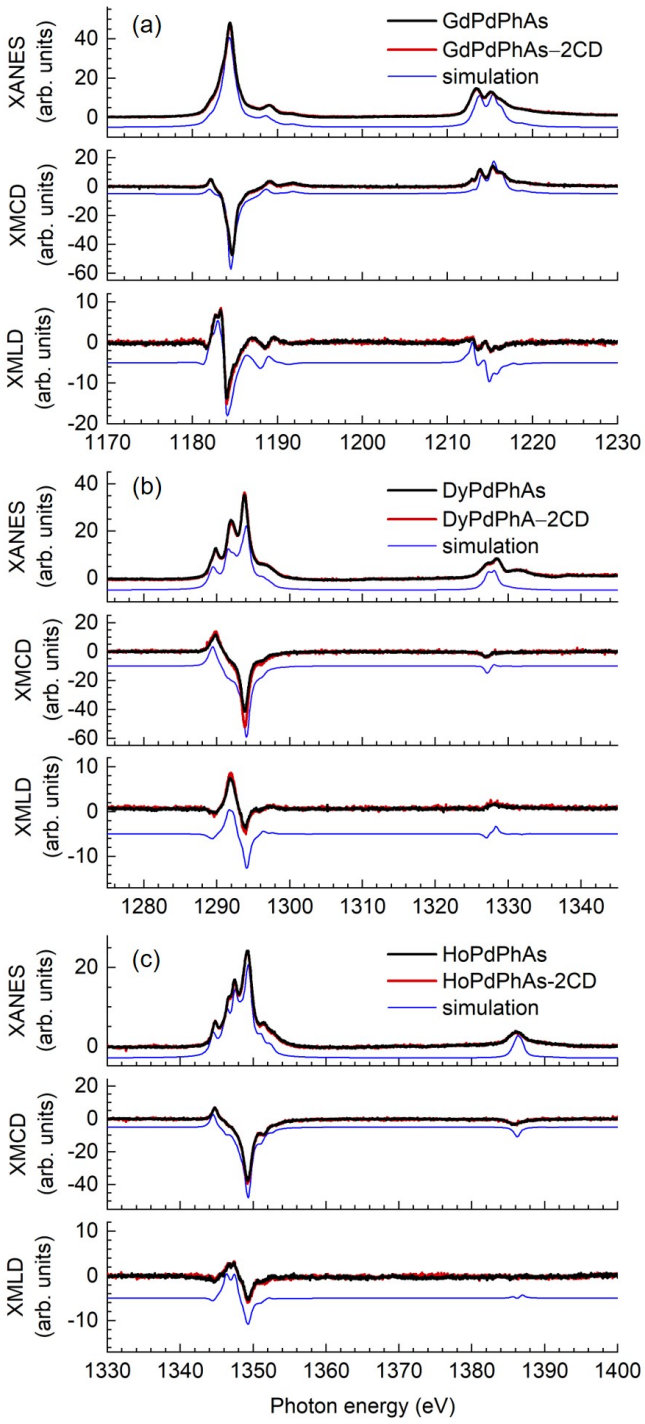

Figure 7: Experimental isotropic x-ray absorption near-edge structure (XANES), magnetic circular dichroism (XMCD), and magnetic linear dichroism (XMLD) for LnPdPhAs (black lines) and LnPdPhAs-2CD (red lines) at $T = 4.7$ K and $B = 6$ T. (Ln = Gd (a), Dy (b), Ho (c).) Blue lines represent corresponding simulated spectra of Gd^{3+}, Dy^{3+}, and Ho^{3+} and are vertically shifted for clarity.

For the case of Gd^{3+}, isotropic XANES, XMCD, and XMLD spectra of GdPdPhAs and GdPdPhAs-2CD remain largely unchanged within experimental uncertainties. The XMCD is negative at the M_5 absorption edge and positive at the M_4 edge with approximately the same integrated intensities corresponding to a dominating spin contribution to the total magnetic moment. In fact, integration of the XMCD signal approaches zero in agreement to the vanishing orbital magnetic moment for the parental POP and is very close to zero after attachment of the CD molecules (see Supporting Material).

The large orbital contribution of Dy^{3+} leads to a negative XMCD peak at the corresponding M_4 absorption edge. Furthermore, some small changes were obtained when comparing the spectra of DyPdPhAs and DyPdPhAs-2CD: Having a look at the three peaks of the M_5 absorption edge around 1290 eV, a change in the relative intensities is visible. More specifically, the relative intensity of the second peak is reduced after attaching CD molecules. The negative main XMCD peak is enhanced as well as the XMLD. In the case of HoPdPhAs, a similar effect is obtained but the differences are smaller compared to the case of Dy^{3+} central ions. Before turning to the discussion of a possible influence of the crystal field on the 4f states, some experimental pitfalls shall be mentioned (and excluded for this work) that may lead to a misinterpretation.

The spectral shape can be changed because of technical artifacts such as crystallite alignment while ramping the magnetic field as already discussed for magnetometry measurements, temperature, charging and saturation/self-absorption effects. Crystallites alignment of the POP deposited on HOPG by rotation in the applied magnetic field cannot be excluded completely, but is unlikely since the adhesion between POP with PhAs capping groups and HOPG is quite large as could be seen from the coverage behaviour during drop coating. Thermal population of different states potentially influences the fine structure. But the temperature was monitored and recorded during the measurements and was the same for all spectra presented. Since the samples with the parental POP and the corresponding CD modified species were mounted on the same sample holder, even dropped on different positions of the same HOPG crystal, a temperature difference by different thermal contacts between cryostat and sample can be excluded as well. Nevertheless, in Fig. S12 of the Supplementary Material we present calculated spectra for Dy^{3+} at $T = 5\,\mathrm{K}$ and $T = 50\,\mathrm{K}$. No change in the spectral shape is visible.

Artificial spectral features can also be induced by (de-)charging. If the electric conductivity of the sample is not sufficiently high for measuring the total electron yield, not only slow background changes and spikes caused by spontaneous discharging can occur. In addition, the amplitudes can be reduced and the peaks artificially broadened as shown in Fig. S5 of the Supplementary Material for the example of GdPdPhAs powder sample on adhesive carbon tape. In our case, the conductivity is generally worse for the sample with CDs attached. However, the coverage was very low and no additional peak broadening is visible. In addition, self-absorption and saturation effects [24]

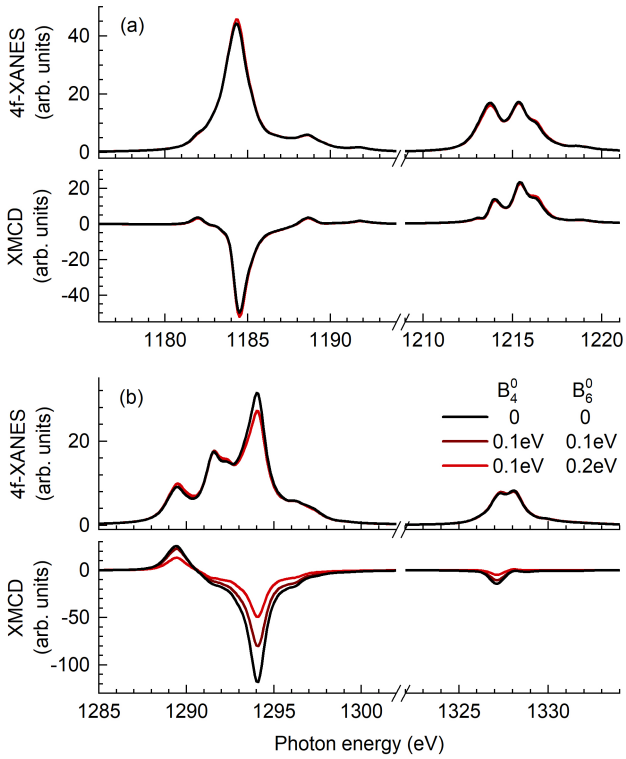

Figure 8: Simulated isotropic x-ray absorption near-edge structure (4f-XANES) and magnetic circular dichroism (XMCD) for Gd^{3+} (a) and Dy^{3+} (b) for different crystal fields. The same scalings were used as in Fig. 7.

can be excluded in this geometry (normal incidence) with the low coverage used here. Therefore, all obvious technical problems are excluded.

To investigate whether the small changes can be related to a different crystal field, the changes were compared to calculated initial-state properties and excitation spectra either without considering a crystal field as presented in the previous subsection or with a crystal field described by $B_4^0 = 0.1\,\mathrm{eV}$ and $B_6^0 = 0.1\,\mathrm{eV}$ or $0.2\,\mathrm{eV}$. It can clearly be seen in Fig. 8 that the 4f states of Gd^{3+} remain largely unaffected by the crystal field, while for Dy^{3+} the crystal field yields obviously different intensities of the fine structure at the M_5 absorption edge and a significantly reduced XMCD. Hence, the experimental findings are qualitatively supported. Furthermore, the cubic field caused by eight oxygen anions was already identified as a promising symmetry for modifications of the 4f states [25].

The calculated expectation values $\langle J_z \rangle$, $\langle S_z \rangle$, $\langle L_z \rangle$, $\langle T_z \rangle$ for two cases, without and with crystal field, are presented in Table 5. They were calculated as sums of $\mathrm{d}Z$ weighted values of thermally populated eigenstates with $\mathrm{d}Z > 1\,\%$ without crystal field and in octahedral (O_h) environment with

Ion	B_4^0 (eV)	B_6^0 (eV)	$\langle J_z \rangle$	$\langle L_z \rangle$	$\langle S_z \rangle$	$\langle T_z \rangle$
Gd^{3+}	-	-	-3.25	-0.03	-3.22	0.01
Gd^{3+}	0.1	0.2	-3.25	-0.03	-3.22	0.01
Dy^{3+}	-	-	-6.93	-4.70	-2.23	0.12
Dy^{3+}	0.1	0.2	-3.37	-2.20	-1.17	0.05
Ho^{3+}	-	-	-7.41	-5.63	-1.77	-0.13
Ho^{3+}	0.1	0.2	-5.19	-3.85	-1.34	-0.08

Table 5: Calculated expectation values $\langle J_z \rangle$, $\langle S_z \rangle$, $\langle L_z \rangle$, $\langle T_z \rangle$ for experimental conditions, i.e. $T = 5\,\mathrm{K}$, $B_z = 6\,\mathrm{T}$. The values have been calculated as sums of dZ weighted values of thermally populated eigenstates with d$Z > 1\,\%$ without crystal field and in octahedral (O_h) environment. Full lists of states can be found in Tables S1-S3 of the Supplementary Material.

	m_s^{eff} (μ_B)	m_l (μ_B)	m_{tot} (μ_B)	m_l/m_s^{eff}
theo. $Gd^{3+}(O_h)$	6.41	0.03	6.44	≈ 0
GdPdPhAs	6.31 ± 0.8	≈ 0	6.31 ± 0.8	≈ 0
GdPdPhAs-2CD	6.28 ± 0.8	0.09 ± 0.05	6.37 ± 0.8	≈ 0
theo. $Dy^{3+}(O_h)$	2.19	2.20	4.39	1.00
DyPdPhAs	1.72 ± 0.4	2.17 ± 0.2	3.89 ± 0.4	1.2 ± 0.2
DyPdPhAs-2CD	2.39 ± 0.5	2.57 ± 0.3	4.96 ± 0.5	1.1 ± 0.3
theo. $Ho^{3+}(O_h)$	2.92	3.85	6.77	1.31
HoPdPhAs	2.91 ± 0.6	2.86 ± 0.3	5.77 ± 0.6	1.0 ± 0.3
HoPdPhAs-2CD	2.89 ± 0.6	3.01 ± 0.3	5.90 ± 0.6	1.0 ± 0.3

Table 6: Effective spin, orbital and total magnetic moment as well as ratio of orbital to effective spin magnetic moment from experimental data and calculations.

$B_4^0 = 0.1\,\mathrm{eV}$ and $B_6^0 = 0.2\,\mathrm{eV}$. Full lists of states can be found in Tables S1-S3 of the Supplementary Material. The 4f states of Gd^{3+} remain unaffected by the crystal field. As a general trend for Dy^{3+} and Ho^{3+} it can be summarized that all expectation values are reduced by the crystal field.

Experimental magnetic moments determined by a sum-rule based analysis are presented in Table 6 and compared to corresponding values derived from theory. Note that the application of sum rules to the $M_{5,4}$ absorption edges of lanthanides suffers from mixing of the initial states due to $3d - 4f$ exchange interaction and $3d$ spin-orbit interaction. The intrinsic line broadening follows a Fano line shape rather than a Lorentzian leading to non-vanishing contributions between the M_5 and M_4 absorption edges. Since for the late 4f elements the corrections are usually less than 10% [22], we present the results of a straight-forward sum rule analysis in Table 6. The integrals of XMCD and 4f-XANES and a description of data treatment are presented in the Supplementary Material.

For GdPdPhAs the experimental effective magnetic moment is $(6.31 \pm 0.8)\,\mu_B$ and the orbital magnetic moment is zero as expected from the $4f^7$ electron configuration, which is also in good agreement with the values obtained from theory. The magnetic moments of GdPdPhAs-2CD are the same within experimental uncertainties. A tiny orbital magnetic moment may be present but has to be verified or falsified by further investigations. DyPdPhAs exhibits an effective spin magnetic moment of $(1.72 \pm 0.4)\,\mu_B$ and a larger orbital magnetic moment of $(2.17 \pm 0.2)\,\mu_B$, which is also in reasonable agreement with theoretical results for Dy^{3+} in a crystal field. Without considering the crystal field, the calculated magnetic moments are significantly too large. DyPdPhAs-2CD has larger effective spin and orbital magnetic moments as the parental POP, which has already been qualitatively concluded from the increased XMCD signal. The changes of the magnetic moments and the fine structure of isotropic XANES indicate a measurable influence of the symmetry distortion by the two CD molecules on the magnetism of the Dy 4f states. The effective spin magnetic moment of HoPdPhAs is $(2.91 \pm 0.6)\,\mu_B$ and in agreement with the calculated one considering a crystal field. Again, without crystal field the theoretical magnetic moment is too large. The experimental orbital magnetic moment of $(2.86 \pm 0.3)\,\mu_B$ is smaller than the calculated value. This may simply indicate that the crystal field was not chosen correctly. A reliable determination of crystal field parameters needs further investigations, preferentially with different methods, and is beyond the scope of this paper.

6. Summary and Conclusion

It has been shown that x-ray absorption spectroscopy is a powerful tool to monitor changes in the electronic and/or magnetic properties of both d metal and lanthanide ions induced by crystal field effects. In particular, (i) orbital re-occupation of Co^{2+} due to different coordination symmetries leads to a significant change of the total magnetic moment as well as of the intensity and

spectral shape of the magnetic linear dichroism. In the case of 4f states of trivalent lanthanide ions it was shown that Gd^{3+} remains largely unaffected by a crystal field, while Dy^{3+} and Ho^{3+} show a measurable influence of an octahedral crystal field that yields significantly reduced magnetic moments with respect to the free ion values. In addition, the 4f states of Dy^{3+} and Ho^{3+} show sensitivity to an axial distortion caused by two trans-positioned CD molecules attached. These results show that x-ray absorption spectroscopy is useful to identify and characterize suitable candidates for single molecular magnets or qubits, whose magnetic properties can be tailored by crystal field modifications.

7. Acknowledgement

We thank the Helmholtz-Zentrum Berlin (HZB) for the allocation of synchrotron radiation beamtime and access to the laboratory for magnetic measurements of the CoreLab Quantum Materials. For kind support we thank the HZB staff, particularly E. Weschke and E. Schierle. F.M.F de Groot (Utrecht U.) is gratefully acknowledged for helpful discussions. This work was partly funded by the Helmholtz Association (VH-NG-1031).

References

[1] E. V. Chubarova, M. H. Dickman, B. Keita, L. Nadjo, F. Miserque, M. Mifsud, I. W. Arends, U. Kortz, Self-Assembly of a Heteropolyoxopalladate Nanocube: $[Pd^{II}_{13}As^{V}_{8}O_{34}(OH)_6]^{8-}$, Angewandte Chemie International Edition 47 (49) (2008) 9542–9546. doi:10.1002/anie.200803527.

[2] E. V. Chubarova, M. H. Dickman, B. Keita, L. Nadjo, F. Miserque, M. Mifsud, I. W. Arends, U. Kortz, Selbstorganisation eines Heteropolyoxopalladat-Nanowürfels, $[Pd^{II}_{13}As^{V}_{8}O_{34}(OH)_6]^{8-}$, Angewandte Chemie 120 (49) (2008) 9685–9689. doi:10.1002/ange.200803527.

[3] S. Bhattacharya, W. W. Ayass, D. H. Taffa, A. Schneemann, A. L. Semrau, S. Wannapaiboon, P. J. Altmann, A. Pöthig, T. Nisar, T. Balster, N. C. Burtch, V. Wagner, R. A. Fischer, M. Wark, U. Kortz, Discovery of Polyoxo-Noble-Metalate-Based Metal-Organic Frameworks, Journal of the American Chemical Society 141 (8) (2019) 3385–3389, doi:10.1021/jacs.8b13397.

[4] C. Schmitz-Antoniak, N. V. Izarova, N. Svechkina, A. Smekhova, M. Stuckart, D. Schmitz, P. Kögerler, Polyoxopalladates as Prototype Molecular Hydrogen Uptake Systems and Novel In situ Hydrogen Detectors on the Nanoscale, European Journal of Inorganic Chemistry 2019 (3-4) (2019) 448–455. doi:10.1002/ejic.201800972.

[5] J. J. Baldoví, L. E. Rosaleny, V. Ramachandran, J. Christian, N. S. Dalal, J. M. Clemente-Juan, P. Yang, U. Kortz, A. Gaita-Ariño, E. Coronado, Molecular spin qubits based on lanthanide ions encapsulated in cubic polyoxopalladates: design criteria to enhance quantum coherence, Inorg. Chem. Front. 2 (2015) 893–897. doi:10.1039/C5QI00142K.

[6] M. Barsukova-Stuckart, N. V. Izarova, R. Barrett, Z. Wang, J. van Tol, H. W. Kroto, N. S. Dalal, B. Keita, D. Heller, U. Kortz, 3d Metal Ions in Highly Unusual Eight-Coordination: The Phosphate-Capped Dodecapalladate(II) Nanocube, Chemistry - A European Journal 18 (20) (2012) 6167–6171. doi:10.1002/chem.201200060.

[7] M. Barsukova, N. V. Izarova, R. N. Biboum, B. Keita, L. Nadjo, V. Ramachandran, N. S. Dalal, N. S. Antonova, J. J. Carbó, J. M. Poblet, U. Kortz, Polyoxopalladates Encapsulating Yttrium and Lanthanide Ions, $[X^{III}Pd^{II}_{12}(AsPh)_8O_{32}]^{5-}$ (X=Y, Pr, Nd, Sm, Eu, Gd, Tb, Dy, Ho, Er, Tm, Yb, Lu), Chemistry - A European Journal 16 (30) (2010) 9076–9085. doi:10.1002/chem.201000631.

[8] M. Barsukova-Stuckart, N. V. Izarova, R. A. Barrett, Z. Wang, J. van Tol, H. W. Kroto, N. S. Dalal, P. Jimnez-Lozano, J. J. Carbó, J. M. Poblet, M. S. von Gernler, T. Drewello, P. de Oliveira, B. Keita, U. Kortz, Polyoxopalladates Encapsulating 8-Coordinated Metal Ions, $[MO_8Pd^{II}_{12}L_8]^{n-}$ ($M = Sc^{3+}$, Mn^{2+}, Fe^{3+}, Co^{2+}, Ni^{2+}, Cu^{2+}, Zn^{2+}, Lu^{3+}; $L = PhAsO_{32}$, $PhPO_{32}$, SeO_{32}), Inorganic Chemistry 51 (24) (2012) 13214–13228, pMID: 23194400. doi:10.1021/ic301537n.

[9] P. Yang, U. Kortz, Discovery and Evolution of Polyoxopalladates, Accounts of Chemical Research 51 (7) (2018) 1599–1608, pMID: 29912555. doi:10.1021/acs.accounts.8b00082.

[10] M. Stuckart, N. V. Izarova, J. van Leusen, A. Smekhova, C. Schmitz-Antoniak, H. Bamberger, J. van Slageren, B. Santiago-Schübel, P. Kögerler, Host-Guest-Induced Environment Tuning of 3d Ions in a Polyoxopalladate Matrix, Chemistry - A European Journal 24 (67) (2018) 17767–17778. doi:10.1002/chem.201803531.

[11] A. Smekhova, D. Schmitz, N. V. Izarova, M. Stuckart, S. F. Shams, K. Siemensmeyer, F. M. F. de Groot, P. Kögerler, C. Schmitz-Antoniak, Intramolecular crossover from 2D diamagnetism to 3D paramagnetism of Pd ions probed by soft x-rays, under consideration (2019).

[12] M. W. Haverkort, M. Zwierzycki, O. K. Andersen, Multiplet ligand-field theory using Wannier orbitals, Phys. Rev. B 85 (2012) 165113. doi:10.1103/PhysRevB.85.165113.

[13] M. W. Haverkort, et al. [link].
URL http://www.quanty.org

[14] M. Retegan, Crispy: v0.7.3 (2019). doi:10.5281/zenodo.1008184.

[15] F. M. F. de Groot, J. C. Fuggle, B. T. Thole, G. A. Sawatzky, 2p x-ray absorption of 3d transition-metal compounds: An atomic multiplet description including the crystal field, Phys. Rev. B 42 (1990) 5459–5468. doi:10.1103/PhysRevB.42.5459.

[16] B. T. Thole, P. Carra, F. Sette, G. van der Laan, X-ray circular dichroism as a probe of orbital magnetization, Phys. Rev. Lett. 68 (1992) 1943–1946. doi:10.1103/PhysRevLett.68.1943.

[17] P. Carra, B. T. Thole, M. Altarelli, X. Wang, X-ray circular dichroism and local magnetic fields, Phys. Rev. Lett. 70 (1993) 694–697. doi:10.1103/PhysRevLett.70.694.

[18] C. T. Chen, Y. U. Idzerda, H.-J. Lin, N. V. Smith, G. Meigs, E. Chaban, G. H. Ho, E. Pellegrin, F. Sette, Experimental Confirmation of the X-Ray Magnetic Circular Dichroism Sum Rules for Iron and Cobalt, Phys. Rev. Lett. 75 (1995) 152–155. doi:10.1103/PhysRevLett.75.152.

[19] E. Goering, S. Gold, M. Lafkioti, G. Schütz, Vanishing Fe 3d orbital moments in single-crystalline magnetite, Europhysics Letters (EPL) 73 (1) (2006) 97–103. doi:10.1209/epl/i2005-10359-8.

[20] A. Abragam, B. Bleaney, Electron Paramagnetic Resonance of Transition Ions, Clarendon, Oxford, 1970.

[21] L. Ungur, L. F. Chibotaru, Ab Initio Crystal Field for Lanthanides, Chemistry - A European Journal 23 (15) (2017) 3708–3718. doi:10.1002/chem.201605102.

[22] Y. Teramura, A. Tanaka, B. Thole, T. Jo, Effect of Coulomb Interaction on the X-Ray Magnetic Circular Dichroism Spin Sum Rule in Rare Earths, Journal of the Physical Society of Japan 65 (9) (1996) 3056–3059. doi:10.1143/JPSJ.65.3056.

[23] J. Stöhr, Exploring the microscopic origin of magnetic anisotropies with X-ray magnetic circular dichroism (XMCD) spectroscopy, Journal of Magnetism and Magnetic Materials 200 (1) (1999) 470 – 497. doi:https://doi.org/10.1016/S0304-8853(99)00407-2.

[24] R. Nakajima, J. Stöhr, Y. U. Idzerda, Electron-yield saturation effects in L-edge x-ray magnetic circular dichroism spectra of Fe, Co, and Ni, Phys. Rev. B 59 (1999) 6421–6429. doi:10.1103/PhysRevB.59.6421.

[25] S. F. A. Kettle, A. J. Smith, The stereochemistry of metal complexes as an indication of f-orbital participation in the metal-ligand bonding, J. Chem. Soc. A (1967) 688–692doi:10.1039/J19670000688.